Stereoscopic Passive Millimeter-Wave Imaging and Ranging

Thomas Lüthi and Christian Mätzler, *Senior Member, IEEE*

Abstract—This paper presents the first stereoscopic range measurements at a wavelength of 3.3 mm and discusses the accuracy of this new method. The synthesis of passive millimeter-wave imaging and stereoscopy combines the advantages of both principles, naturally looking high-contrast images and superior poor-weather performance (compared to visible and infrared wavelengths), as well as the passive ranging capability. Our setup using two antennas with a half-power beamwidth (HPBW) of 0.9° and a stereoscopic baseline of 1.15 m allows ranging with an accuracy of ≈10% up to a distance of ≈300 m. The range resolution improves with increasing stereoscopic baseline, lower radiometer noise, narrower antenna beams, and higher scene contrast. For scenes with sufficient contrast, the directional resolution is considerably better than the antenna HPBW. Thus, massive oversampling of the scene in the plane of the stereoscopic baseline is required. For our setup, an oversampling factor of 36 is optimal. Since additional ranging errors result from nonstationary scenes, fast scanning imagers should be applied.

Index Terms—Distance measurement, millimeter-wave imaging, millimeter-wave technology, radiometry, stereo vision.

I. INTRODUCTION

PASSIVE millimeter-wave imaging has become of increasing interest for scientific, military, and commercial applications over the last years. Millimeter-wave radiation is due to thermal emission from the objects in the scene, thus no illumination is required as for visible light sensors. Attenuation and scattering by fog, clouds, and light drizzle is considerably lower than in the visible and infrared range (except for strong molecular absorption lines, e.g., the complex of oxygen lines at 60, the line at 118, and the water-vapor line at 183 GHz). The contrast in millimeter-wave images is larger by up to two orders of magnitude compared with infrared scenes due to the cold sky emission reflected from metal objects and smooth surfaces (e.g., [1], [2]). Passive millimeter-wave imaging thus produces naturally looking high-contrast thermal images (cf. Section II) and offers superior poor-weather performance compared to visible and infrared systems. Additionally, millimeter waves penetrate most types of clothing and camouflage. The major drawback of millimeter-wave imagers is their lower angular

resolution due to the longer wavelength and limited aperture size. Nevertheless, millimeter-wave imaging systems are currently developed for a wide range of applications including remote sensing, environmental monitoring, aircraft landing aids, and concealed weapon detection (e.g., [3]).

For most of these applications, a detailed two-dimensional image is adequate. However, there are many other applications where the range to an object is also of interest. At microwave and millimeter wavelengths, the main ranging technique is radar, which is an active method. At visible wavelengths, however, ranging is mostly done by passive methods: the three-dimensional human vision is based on stereoscopy. Before the advent of satellite-based positioning systems, cartography and land survey relied on optical triangulation methods. Photogrammetric methods using a large number of images taken from different locations allow the three-dimensional reconstruction of objects with an accuracy of up to a few micrometers (e.g., [4]).

A synthesis of passive millimeter-wave imaging and stereoscopy combines the advantages of both principles, high-contrast images, and superior poor-weather performance, as well as passive ranging capability. Besides the fact that passive systems benefit from better public acceptance and are well preferred for military applications as they are difficult to locate, ranging the distance to a remote object with a pair of passive imagers is quite different from ranging with active sensors such as a radar. Whereas the former uses angular measurements at a given baseline distance (triangulation), the latter uses measurements of propagation time at a given propagation speed. The main advantage of radar is the independence of range resolution from range itself, assuming a constant signal speed. A disadvantage is the occurrence of speckle noise. Detectability problems occur if target shape and size are unknown because the return may either be extremely large or missing at all. As an example, a small number of raindrops may lead to erroneous ranging of clouds with a cloud radar; or in case of an object with specular surfaces, the return signal critically depends on the object orientation. On the other hand, passive imaging is free of speckle noise. Instead, thermal noise limits the object detectability. An important advantage of passive imaging is the fact that object shape and size do not have deteriorating effects. Perhaps the most relevant advantage of passive stereoscopic imaging is based on the measurement of angular differences for positioning in all three dimensions, thus minimizing the occurrence of systematic errors, and allowing the application of super-resolution techniques to suitable objects. This property may be the reason for nature to prefer this sensing method, although active methods are used as well.

According to our knowledge, stereoscopic passive millimeter-wave imaging has not been reported thus far. In order

T. Lüthi was with the Institute of Applied Physics, University of Bern, 3012 Bern, Switzerland. He is now with the I. Physics Institute, University of Köln, 50937 Köln, Germany (e-mail: luethi@ph1.uni-koeln.de).

C. Mätzler is with the Institute of Applied Physics, University of Bern, 3012 Bern, Switzerland.

to demonstrate that the method is quite powerful, stereo-scopic measurements were made with a simple stereoscopic radiometer system at a wavelength of 3.3 mm. In this paper, we present first stereoscopic images, as well as the derived range map, and discuss the ranging accuracy of the new method.

II. EXPERIMENTAL SETUP

Stereoscopic imaging requires either two laterally displaced imagers or one imager taking images sequentially from different locations. However, for most applications, the latter method is not practical as it depends on stationary scenes and constant weather conditions. The imaging process can be achieved by different methods, which include: 1) mechanically scanning a pencil-beam radiometer in two dimensions over the field of view or a linear array of radiometer beams in one dimension (e.g., [5], [2]); 2) using a fixed two-dimensional array of radiometers in the focal plane of an optical system [6]; 3) electronically scanning the beam of a two-dimensional antenna array by inserting time lags into the signal path prior to combination (e.g., [1]); 4) using a linear array of frequency-directive antennas [7]; or 5) synthesizing the image from the visibility functions of an interferometer [8].

Most of these imaging systems are still under development or exist only as prototypes. However, practical stereoscopic imaging requires at least two imagers. Such a system resulted as a by-product from our Nulling Interferometer for the Observation of Solar flares at 90 GHz (NIOS; [9], [10]). In order to improve the sensitivity for the detection of weak solar flares, this instrument suppresses the strong quiet Sun background emission by correlating the signals from two small antennas (destructive interference). Both antennas are installed on a common mount of a single tracker to preserve the effective antenna baseline D of 1.15 m, while the position of the Sun changes throughout the day (Fig. 1). Besides the complex correlation of the antenna signals, the total power signals detected by the two antennas are also recorded. These signals were used for stereoscopic imaging. The sensitivity of the radiometers is 0.5 K at an integration time constant τ_{RC} of 31 ms (Table I). There is no internal calibration system, as the solar observations use the cold sky and the quiet Sun as natural calibration references. Stereoscopic imaging was done during the night without radiometric calibration.

The half-power beamwidth (HPBW) of the antennas (and, thus, the angular resolution of the instrument) is 0.9° (optimized for solar flare observations). Images were obtained by mechanically scanning the scene (i.e., method 1). As the front-end is mounted on the elevation axis of the elevation-over-azimuth tracker, the main scan direction for stereoscopic imaging was in elevation. This ensures that the same feature of the scene is seen by both antennas within a few seconds, thus minimizing the effect of instrumental drifts and changing weather conditions. Furthermore, the fixed mounting of the antennas on a common bar ensures a constant baseline independent on the view direction, and eliminates relative tracking errors between the two antennas.

Nyquist sampling permits a maximum angular distance of $HPBW/2$ between the individual sample points (i.e., image pixels) in order to avoid aliasing effects. Therefore, the distance between vertical scan lines was set to 0.4°. In elevation, however, oversampling is highly advantageous: as long as the contrast in an image is high enough to identify distinct features,
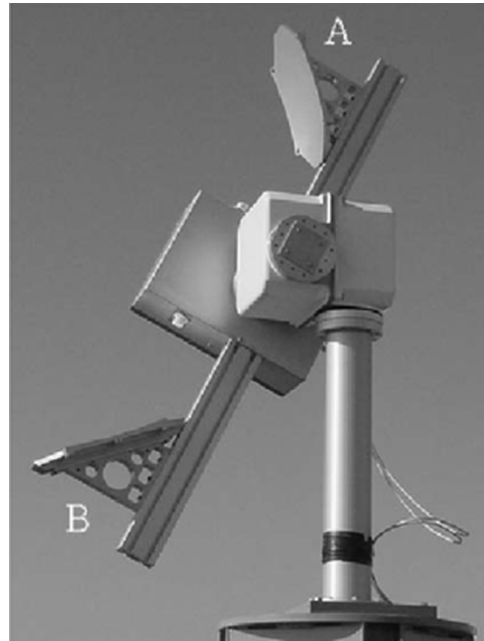

Fig. 1. NIOS front-end with the two antennas A and B installed on a common mount.

TABLE I
NIOS INSTRUMENT SPECIFICATIONS

Observation wavelength	3.3 mm
Polarization	linear (horizontal)
System noise temperature	2800 K
Integration time constant	31 ms
Bandwidth	500 MHz (single sideband mode)
Radiometric sensitivity	0.5 K
Antenna baseline	1.15 m
Antenna Diameter	0.25 m
Antenna HPBW	0.9 deg
Max. scanning speed	0.2 deg/s

they can be localized with a much better accuracy than the angular resolution of the antenna (cf. Section IV-A). The angular resolution of the tracker is ≈0.04°. However, as it uses dc motors to drive the two axes, the movement of the instrument is continuous, and positions within the same vertical scan line can be interpolated even to a higher resolution. Taking into account the tracking velocity of 0.2°/s, there are ≈150 integration time constants τ_{RC} per HPBW. The images are, therefore, massively oversampled in elevation. In order to reduce noise and computation time, the data is then rebinned for stereoscopy to an image resolution of 1/40° (cf. Section IV-A).

NIOS is installed on top of the science building of the University of Bern, Bern, Switzerland. Located near the city center, the surroundings provide ample objects of different appearance and at different distances in order to assess the ranging performance of the setup. The chosen field of view (110° in azimuth and 15° in elevation) is shown in Fig. 2. It is dominated by the nearby university main building (a) and a distant hill (b). Other prominent features are some trees (c, d), a tall office building (e), and a crane (f). The main feature in the foreground is a radiometer for atmospheric research (g). Scanning time for an image is approximately 6 h.
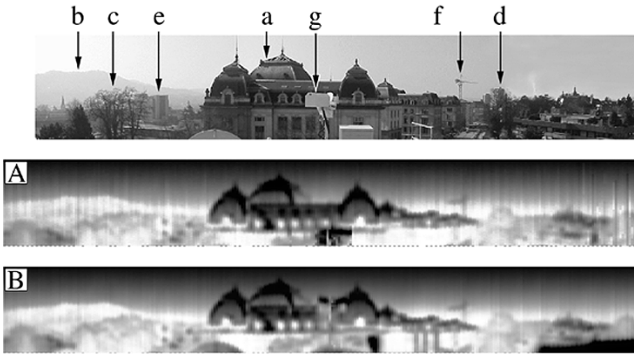
Fig. 2. Visible and millimeter-wave images ($\lambda = 3.3$ mm, "warm" objects appear bright) of the test site, which is dominated by: (a) the university main building and (b) a hill in the background. Other prominent features are: (c) and (d) some trees, (e) an office building, (f) a crane, and (g) a radiometer for atmospheric research. The radio images from the (A) upper and (B) lower antenna clearly show the effects of the different "camera" locations, as objects in the foreground appear at higher elevations in (B).

The millimeter-wave images were histogram equalized in order to enhance contrast. They show a detailed view of the scene. Only the nearby radiometer (g) appears blurred, as it was moving while scanned. Objects with a high brightness temperature appear bright, those with a low brightness temperature dark. The images illustrate the main properties of millimeter-wave images: metal (crane, radiometer) and inclined smooth objects (slate roof and cupolas of the main university building) reflect the cold (zenith) sky, whereas walls (rough sandstone) and vegetation exhibit a high brightness temperature. Due to the increasing optical depth, the brightness temperature of the unobstructed atmosphere increases with decreasing elevation angle, resulting in a bright horizon.

III. STEREOSCOPIC RANGING

The radio images from the (A) upper and (B) lower antenna clearly show the effects of the different "camera" locations, as objects [especially the radiometer (g)] in the foreground appear at higher elevations in image (B). Several low and nearby objects are only imaged with the lower antenna, e.g., part of our own building's roof (lower right-hand-side corner).

The most direct way to analyze stereoscopic images is the use of a stereoscopic viewer, which presents each of the two images exclusively to one eye. Although the view with a vertical stereoscopic baseline (and, thus, a vertical horizon) is somewhat unusual, clearly the impression of a three-dimensional image is obtained.

For a quantitative analysis, two different methods were applied. First quantitative results were obtained by manually selecting corresponding features in both images and determining the resulting parallax α. The stereoscopic distance r is given by

$$r = \frac{D}{2\tan(\alpha/2)} \tag{1}$$

where D is the stereoscopic baseline of 1.15 m. Stereoscopic distances to several prominent features are given in Table II, as well as the true distances r_{true} obtained from a city map (accuracy ≈ 10 m). In general, they agree within $\approx 10\%$, which clearly proves the concept of passive millimeter-wave ranging. However, manually selecting corresponding features is not very practical and prone to error, especially for distant objects where a

TABLE II
STEREOSCOPIC AND TRUE DISTANCES FOR MANUALLY SELECTED OBJECTS (r, r_{true}) AND CORRESPONDING MEAN DISTANCES FROM THE RANGE MAP FIG. 3(e) (r_{map})

Object	r [m]	$r_{\text{map}}[m]$	$r_{\text{true}}[m]$
Radiometer (g)	10	11	9
University main building (windows)	65	65	60
University main building (main cupola)	110	110	105
Tree (c)	120	115	110
Tree (d)	145	165	160
Office building (e)	330	–*	320
Crane (f)	330	390	310

* not recognizable in the range map

minor deviation in elevation results in a large distance error. The method might be improved by the use of a feature-recognition algorithm to identify common objects in the two images. This would not only automate the process and remove the human factor, but also reduce the sensitivity toward noise, as for each identified object, only the center position (i.e., the barycenter of all pixels composing the object) is used for ranging.

The second method analyzes stereoscopic images without any knowledge of the image content by cross-correlation of the two images. A sub-region a of image (A) is selected and correlated with the sub-regions $b_0, b_1, b_2, \ldots,$ of image (B), shifted in elevation. To optimize azimuthal resolution, the sub-regions consist of sections of single vertical scan lines. The shift in elevation for which the correlation is maximum gives the parallax α for the selected sub-region a. We determined the range to any sub-region that exhibited a sufficient contrast, and generated range maps. As the correlation of two signals is invariant with respect to offsets and gain differences, no prior calibration of the two images is required. The algorithm for parallax determination and distance computation was realized in the data visualization and analysis software IDL.

The angular resolution of the resulting range map depends on the size of the sub-regions used for correlation. In order to determine the optimum extent of the sub-region, the process was repeated for different values (Fig. 3). For extents below the HPBW of the antennas, the range map exhibits a considerable "range noise." This becomes especially pronounced in regions of low image contrast like the sky or the distant hill where the image fine structure is mainly due to radiometer noise and, thus, random ranges are obtained. A sub-region length of two HPBWs, on the other hand, results in a less noisy, but flat-looking range map. Therefore, the optimum sub-region length appears to be in the order of one antenna HPBW.

The resulting range map [see Fig. 3(c)] clearly shows the main features of the scene like the distant hill, the trees on the left-hand side, and the university main building. Note that the different distances to the wall and to the main cupola are well resolved. However, there is still noticeable "range noise." Several numerical methods to reduce this disturbing effect were tested. Best results were obtained with a statistical approach. A real object must be composed of several pixels in the range map at approximately the same distance. Therefore, all range points were discarded for which the relative standard deviation $\Delta r/r$ of the measured range in a region of $0.8° \times 0.8°$ (i.e., $\sim$ the half-power antenna beam) around the range point of interest exceeds 60%.
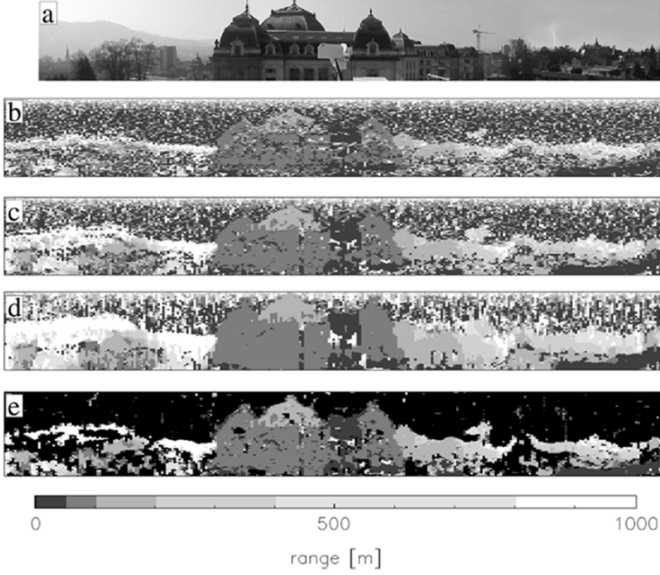
Fig. 3. Grayscale-coded range maps: (a) visible image for reference. Range maps for different sub–region lengths of: (b) 0.5, (c) 1, and (d) 2 antenna HPBWs. The optimum result is achieved for a length of one HPBW (c). Note that the different distances to the wall and main cupola of the university main building are well resolved. Also shown is: (e) the noise-reduced range map. All objects at longer distances than 800 m appear white, whereas black regions in panel (e) represent range points discarded due to excessive range noise.

This approach suppresses the "range noise" effectively. It also discards valid range points at the rim of an object where the range actually exhibits a rapid change. To avoid this problem, all range points were accepted in a second step if they were situated on an edge of the original image. Edges were identified by the Sobel algorithm [11]. The resulting range map [see Fig. 3(e)], where the discarded range points are displayed in black, clearly shows a considerable reduction of the "range-noise." In particular, the crane stands out much more clearly. Mean distances r_{map} to several prominent features are given in Table II. Like the manually determined distances r, they agree well with the true distances r_{true}, except for the office building [see Fig. 2, feature (e)], which is not recognizable in the range map, and the crane [see Fig. 2, feature (f)] whose distance is overestimated by $\approx 25\%$.

IV. ERROR ASSESSMENT

First measurements showed that our setup achieves a ranging accuracy of $\approx 10\%$ up to a distance of ≈ 300 m (Table II). In the following, the accuracy of the method is investigated in more detail.

A. Noise Error

As the direction to an object can be determined with only a limited angular resolution $\Delta\alpha$, the range resolution is also limited. From (1), we obtain for the range error

$$|\Delta r| = \frac{D\Delta\alpha}{4\tan^2(\alpha/2)\cos^2(\alpha/2)}$$
$$= \frac{r^2\Delta\alpha}{D\cos^2(\alpha/2)}$$
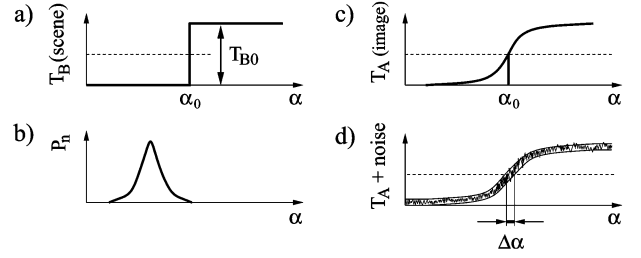$$\approx \frac{r^2\Delta\alpha}{D}, \qquad \alpha \ll 1. \qquad (2)$$

Fig. 4. Effect of radiometer noise on the directional resolution $\Delta\alpha$. Panel (a) shows a simplified brightness temperature distribution T_B, (b) the normalized antenna pattern P_n ($\max(Pn) = 1$), and (c) and (d) the image without and with radiometer noise, respectively.

The range error Δr thus scales with the inverse of the stereoscopic baseline D, directional resolution $\Delta\alpha$, and rapidly degrades with increasing range. For our setup ($D = 1.15$ m, image rebinned to $1/40°$ in elevation), we find a relative range error $\Delta r/r$ of 10% at a distance of 260 m. An improvement of the range resolution may be achieved either by an increase of the stereoscopic baseline D or by an improved directional resolution $\Delta\alpha$. The baseline is quite limited for a mobile device (e.g., like a system for automobile distance detection) due to practical reasons. For a fixed installation like a system for airport taxiway and apron area surveillance, however, it could be extended considerably by the use of two independent millimeter-wave imagers. Independent "cameras" would also allow the application of more than two imagers in order to avoid "blind spots" due to buildings or other fixed structures in the area of surveillance, and to perform multiple stereoscopy for redundancy and increased accuracy.

There are several parameters that limit the directional resolution $\Delta\alpha$ of a scanning radiometer. For a quantitative analysis, we assume a symmetrical antenna pattern and a simple one-dimensional scene where the brightness temperature distribution $T_B(\alpha)$ is a Heaviside function with the step amplitude T_{B0} at the position α_0 [see Fig. 4(a)]. The image obtained with a scanning radiometer (i.e., the antenna temperature $T_A(\alpha)$) corresponds to the convolution between T_B and the normalized antenna pattern P_n [see Fig. 4(b), $\max(Pn) = 1$]

$$T_A(\alpha) = \frac{1}{\Omega_A}\int_{-\infty}^{\infty} P_n(\alpha' - \alpha)T_B(\alpha')\,d\alpha'$$
$$= \frac{T_{B0}}{\Omega_A}\int_{-\infty}^{\alpha-\alpha_0} P_n(u)\,du, \qquad (3)$$

where

$$\Omega_A = \int_{-\infty}^{\infty} P_n(\alpha)\,d\alpha. \qquad (4)$$

is the (one-dimensional) beam solid angle of the antenna. For a symmetrical antenna pattern, we have $T_A(\alpha_0) = T_{B0}/2$, independent of the beamwidth [see Fig. 4(c)]. Therefore, the step position α_0 can be determined exactly in absence of radiometer

noise. However, the presence of noise hampers the measurements, and the position of the imaged step can be retrieved only with an uncertainty $\Delta\alpha$ [see Fig. 4(d)]. In order to quantify this effect, we calculate the derivative of the antenna temperature at the position α_0

$$\frac{d}{d\alpha}T_A(\alpha)\bigg|_{\alpha=\alpha_0} = \frac{T_{B0}}{\Omega_A}P_n(\alpha-\alpha_0)\bigg|_{\alpha=\alpha_0} = \frac{T_{B0}}{\Omega_A} \quad (5)$$

and, finally, obtain the directional error due to noise

$$\Delta\alpha_N = \Omega_A\frac{\Delta T}{T_{B0}} \quad (6)$$

where ΔT is the radiometric sensitivity of the imager (rms). The directional error $\Delta\alpha_N$ thus decreases with increasing contrast T_{B0}, with decreasing ΔT, and with a decreasing beam solid angle. The latter can be approximated with the antenna HPBW and is given by

$$\Omega_A \propto \frac{\lambda}{d_a} \quad (7)$$

where λ is the wavelength and d_a is the antenna diameter. However, both the antenna size and observation wavelength are limited; the former by practical considerations (available space, weight, costs, and scanning speed), and the latter by the properties of the atmosphere. Even in the relevant atmospheric transmission windows at millimeter and submillimeter wavelengths, the sky brightness temperature increases with frequency, thus decreasing the scene contrast T_{B0} [1].

The first stereoscopic images obtained with NIOS clearly showed that, even with a nonoptimized setup, a directional resolution considerably better than the antenna HPBW is obtained. In order to make use of this super-resolution effect, it is essential that the image is oversampled in the plane of the stereoscopic baseline, otherwise the directional resolution will be limited by the spatial sampling rate. For a scanning radiometer, the optimum oversampling factor k_{opt} is given by

$$k_{\mathrm{opt}} \doteq \frac{\mathrm{HPBW}}{\Delta\alpha_N} \approx \frac{\Omega_A}{\Delta\alpha_N} = \frac{T_{B0}}{\Delta T}. \quad (8)$$

The integration time per image pixel thus becomes

$$\tau = t_{\mathrm{HPBW}}/k_{\mathrm{opt}} \quad (9)$$

where t_{HPBW} is the time allotted to scan a distance of one HPBW (i.e., defines the scanning velocity). The radiometric sensitivity of the imager is thus [12]

$$\Delta T = \frac{T_n + \overline{T_{\mathrm{scene}}}}{\sqrt{2\Delta\nu t_{\mathrm{HPBW}}/k_{\mathrm{opt}}}} \quad (10)$$

where T_n is the system noise temperature of the radiometer, $\overline{T_{\mathrm{scene}}}$ is the mean scene brightness temperature, and $\Delta\nu$ is the instrument bandwidth. Combining (8) and (10), we finally obtain

$$k_{\mathrm{opt}} = \left(\frac{T_{B0}\sqrt{2\Delta\nu t_{\mathrm{HPBW}}}}{T_n + \overline{T_{\mathrm{scene}}}}\right)^{2/3}. \quad (11)$$

For the radiometer parameters of our setup (Table I), a scene contrast T_{B0} of 10 K and a mean scene brightness temperature of 290 K, an oversampling factor of $k_{\mathrm{opt}} = 36$ is required. This corresponds to 40 pixels/deg, as chosen for the rebinning of our test images. Realistic scenes are more complex than the one used for the above calculations. There may be several objects or brightness temperature changes, which are smaller than the antenna HPBW, leading to a reduction of the image contrast (after convolution) and, hence, an increase of the directional error $\Delta\alpha_N$ (6). Additionally, a typical scene is composed of objects with different contrasts, leading to a variable directional (and, thus, range) resolution over the scene. The choice of the optimum oversampling factor thus strongly depends on the actual scene and the anticipated scene contrasts.

B. Systematic Errors

The key to an optimal ranging performance is based on a small value of $\Delta\alpha$ (2). As long as (6) completely determines this quantity, the presented analysis can be used for the optimization. However, in order not to limit the directional resolution artificially, it is essential that the spatial sampling rate in the plane of the stereoscopic baseline is at least $1/\Delta\alpha_N$. Additional errors may occur to $\Delta\alpha$ in systems where the two imagers are tracked independently

$$\Delta\alpha = \sqrt{\Delta\alpha_N^2 + 2\Delta\alpha_t^2} \quad (12)$$

where $\Delta\alpha$ is the resulting increased directional error and $\Delta\alpha_t$ is the pointing error of the trackers. Both of the above problems are avoided with our test setup. The slowly and continuously running dc motors of the tracker allow both a very high spatial sampling rate and accuracy within the same vertical scan line, and there are no tracking errors between the two imagers as the angle between the two antennas remains constant.

Furthermore, ranging errors occur if the scene and/or the stereoscopic imaging system is in motion. Any motion parallel to the scan direction leads to an error of the measured parallax α_{meas}

$$\alpha_{\mathrm{meas}} = \alpha_{\mathrm{true}}\frac{\omega_{\mathrm{scan}}}{\omega_{\mathrm{scan}} \mp \omega_{\mathrm{obj}}} \quad (13)$$

where α_{true} is the true parallax, ω_{scan} is the angular scanning velocity, and ω_{obj} is the angular velocity of the object of interest in the plane of the baseline. The "$-$" sign applies to an object moving in the same direction as the scanner, leading to an overestimation of the parallax and, thus, to an underestimation of the range. The resulting range error increases with increasing angular velocity of the moving object and decreasing angular scanning velocity.

In order to quantitatively assess this error, we assume a hypothetical system for airport taxiway and apron area surveillance consisting of several individual rotating scanners with 0.2 turns/s ($\omega_{\mathrm{scan}} = 72°\ \mathrm{s}^{-1}$). From numerical simulations for a taxiing aircraft with a transverse velocity of 20 ms^{-1}, we find a range error of $\sim$16 m, which is almost independent of the actual range to the moving object and the stereoscopic baseline. This is quite acceptable for such an application, especially at longer ranges above a few hundred meters. Additionally, if

the same object is observed in several consecutive scans, its transverse velocity can be estimated and taken into account for the ranging process.

V. CONCLUSION

Passive millimeter-wave imaging was combined with the well-known principle of stereoscopy. The new method offers the advantages of both millimeter-wave imaging systems (high-contrast thermal images and a superior poor-weather performance compared to visible and infrared wavelengths) and passive devices (free of speckle noise, positioning in all three dimensions, not easily located).

First stereoscopic millimeter-wave images were obtained at a wavelength of 3.3 mm and demonstrated that the method is quite powerful. Although our experimental setup did not use state-of-the-art passive millimeter-wave imagers (low radiometric sensitivity and angular resolution), a ranging accuracy of $\approx 10\%$ up to a distance of ≈ 300 m was achieved. Important for this good result is the fixed mounting of the antennas on a common bar, which ensures a constant baseline independent on the view direction, and eliminates relative tracking errors between the two antennas. The range of the imaged objects was computed either by manually selecting the same feature in both images or by cross-correlation of the two millimeter-wave images. The resulting range maps allowed clear discrimination of objects at different distances. Stereoscopic ranging works best for a scene with high brightness temperature contrasts, and where the different objects are large compared with the antenna HPBW. In regions of low scene contrast, the radiometer noise dominates the image fine structure, leading to considerable "range noise." However, the latter can be effectively suppressed by a statistical method analyzing the local relative standard deviation $\Delta r/r$ of the measured range.

In contrast to radar, the range error of stereoscopic ranging methods increases with increasing range to the objects of interest. It decreases with increasing stereoscopic baseline and directional resolution. Whereas the baseline is easily increased by the use of two individual imagers, the directional resolution improves with lower radiometer noise, narrower antenna beams and higher scene contrast. For scenes with sufficient contrast, the directional resolution is considerably higher than the antenna HPBW. Thus, a massive oversampling of the scene in the plane of the stereoscopic baseline is required. For our setup, the optimum oversampling factor is 36, corresponding to a directional resolution of $1/40°$. With a large stereoscopic baseline, a practical range resolution can already be obtained using small antennas with broad beams, although at the cost of a poor angular resolution of the resulting range maps.

Additional ranging errors are introduced if the two images are obtained by independent scanning radiometers (due to pointing errors) and if the scene and/or the stereoscopic imaging system is in motion. The resulting distance error increases with increasing angular velocity of the moving object and decreasing angular scanning velocity. Stereoscopic passive millimeter-wave imaging and ranging thus requires scanning radiometers with fast scanners in the plane of the stereoscopic baseline.

REFERENCES

[1] D. G. Gleed, R. Appleby, N. A. Salmon, S. Price, G. N. Sinclair, R. N. Anderton, J. R. Borill, and M. R. M. Wasley, "Operational issues of passive millimeter wave imaging systems," in *Proc. SPIE Passive Millimeter-Wave Imaging Technology*, vol. 3064, Apr. 1997, pp. 23–33.

[2] A. Pergande, D. Dean, and D. O'Donnell, "Passive millimeter wave imaging," in *Proc. SPIE Enhanced and Synthetic Vision*, vol. 2736, May 1996, pp. 240–247.

[3] *Proc. SPIE Passive Millimeter-Wave Imaging Technology IV*, vol. 4032, R. M. Smith and R. Appleby, Eds., Apr. 2000.

[4] M. Miller, U. U. Graf, R. Kinzel, C. Kramer, M. Lettau, K. Stenvers, and J. Stutzki, "Photogrammetric surface measurement of the KOSMA 3m-telescope," in *Proc. SPIE Millimeter and Submillimeter Detectors for Astronomy*, vol. 4855, Feb. 2003, pp. 594–601.

[5] R. Smith, B. Sundstrom, B. Belcher, and D. Ewen, "ROSCAM A 95 GHz radiometric one second camera," in *Proc. SPIE Passive Millimeter-Wave Imaging Technology II*, vol. 3064, Apr. 1997, pp. 2–13.

[6] L. Yujiri, H. Agravante, S. Fornaca, B. Hauss, R. Johnson, R. Kuroda, B. Quon, A. Rowe, T. Samec, M. Shoucri, and K. Yokoyama, "Passive millimeter wave video camera," in *Proc. SPIE Passive Millimeter-Wave Imaging Technology II*, vol. 3378, Apr. 1998, pp. 14–19.

[7] J. A. Lovberg, R.-C. Chou, and C. A. Martin, "Real-time millimeter-wave imaging radiometer for avionic synthetic vision," in *Proc. SPIE Sensing, Imaging, and Vision for Control and Guidance of Aerospace Vehicles*, Apr. 1994, pp. 234–244.

[8] M. Peichl, H. Suess, M. Suess, and S. Kern, "Microwave imaging of the brightness temperature distribution of extended areas in the near and far field using two-dimensional aperture synthesis with high spatial resolution," *Radio Sci.*, vol. 33, pp. 781–801, 1998.

[9] T. Lüthi, "Nulling interferometer for solar flare observations at 90 GHz," M.Sc. thesis, Inst. Appl. Phys., Univ. Bern, Bern, Switzerland, 1999.

[10] T. Lüthi, "Solar flares at millimeter and submillimeter wavelengths—Instrumental techniques and observations," Ph.D. dissertation, Inst. Appl. Phys., Univ. Bern, Bern, Switzerland, 2004.

[11] R. C. Gonzalez and P. Wintz, *Digital Image Processing*. Reading, MA: Addison-Wesley, 1977, pp. 337–338.

[12] K. Rohlfs and T. L. Wilson, *Tools of Radio Astronomy, Second completely Revised, and Enlarged Edition*. New York: Springer, 1996, Astronomy and Astrophysics Library, pp. 60–64.

Thomas Lüthi was born in Herzogenbuchsee, Switzerland, in 1974. He received the M.S. and Ph.D. degrees in physics from the University of Bern, Bern, Switzerland, in 2000 and 2004, respectively.

He is currently with the I. Physics Institute, University of Köln, Köln, Germany. His research concerns submillimeter-wave instrumentation, quasi-optical antenna systems, and microwave technology.
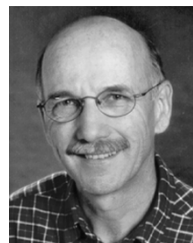
Christian Mätzler (M'96–SM'03) received the M.S. and Ph.D. degrees in physics from the University of Bern, Bern, Switzerland, in 1970 and 1974, respectively.

He was involved with solar radio astronomy and performed post-doctoral studies with the NASA Goddard Space Flight Center and at ETH, Zürich, Switzerland. He is currently Titular Professor of applied physics and remote sensing with the Institute of Applied Physics, University of Bern, where he leads the Project Group Radiometry for Environmental Monitoring. Since 1979, his experimental studies have been concentrated on surface-based microwave (1–100 GHz) signatures for active and passive microwave remote sensing of snow, ice, soil, vegetation, and atmosphere including precipitation, clouds, and the boundary layer, and on the development of methods for dielectric measurements of these media with complementary work at optical wavelengths. He is interested in meteorological applications of remote sensing and in improvements of the physical understanding of the processes involved. Based on the experimental work of his group, he has developed and tested microwave (1–100 GHz) propagation, transmission, emission, scattering, and dielectric models of snowpacks and of the atmosphere.